Pramana – J. Phys. (2019) 93:72
https://doi.org/10.1007/s12043-019-1835-y

Analysis with relativistic mean-field density distribution of elastic scattering cross-sections of carbon isotopes ($^{10–14,16}$C) by various target nuclei

M AYGUN

Department of Physics, Bitlis Eren University, 13000 Bitlis, Turkey
E-mail: murata.25@gmail.com

MS received 25 October 2018; revised 17 April 2019; accepted 31 May 2019

Abstract. A microscopic study of elastic scattering of carbon isotopes from different target nuclei at various incident energies is presented by using density distributions derived for $^{10–14,16}$C nuclei using relativistic mean field (RMF) theory. To obtain the real part of the optical potential, the double folding model is used. Woods–Saxon potential is used for the imaginary part. The theoretical results are discussed and compared with each other as well as with the experimental data. It is seen that the agreement between theoretical results and experimental data is very good. Also, new global equations for the imaginary potentials of the $^{10–14,16}$C nuclei are derived from the results of the theoretical analysis.

Keywords. Nuclear reactions; density distributions; elastic scattering.

PACS Nos **24.10.Ht; 25.70.−z**

1. Introduction

Density distribution is a significant output of different nuclear models and plays an important role in the microscopic optical model analysis of nucleon–nucleus and nucleus–nucleus interactions. Density distributions can be found in different shapes [1–7]. However, determining density distributions of nuclei is a major problem and is still an attractive topic in the area of nuclear physics due to the advancement of both theoretical and experimental processes.

Experimental and theoretical surveys on carbon isotopes such as $^{10–14}$C and ^{16}C have been carried out quite intensively. These studies have provided important background information for determining basic nuclear properties such as binding energy, radius and density distributions of carbon isotopes. In this context, we have tried to give some of these reactions that are examined in this study. For example, the scattering cross-sections of the ^{10}C nucleus from ^{27}Al at 29.1 MeV [8] and from ^{208}Pb at 226 MeV [9] were reported. ^{11}C scattering cross-sections off ^{14}N at 110 MeV [10] and ^{208}Pb at 226 MeV [9] were recorded. The scattering cross-sections of ^{12}C projectile on the ^{28}Si, ^{40}Ca, ^{58}Ni, ^{88}Sr, ^{90}Zr and ^{208}Pb nuclei were measured in the 49.3–300 MeV energy range [11–14]. The cross-sections of ^{13}C projectile by the ^{12}C, ^{16}O and ^{28}Si nuclei were carried out by Ikeda *et al* [15], Yamaya *et al* [16] and Berat *et al* [17]. The scattering cross-sections of ^{12}C by ^{13}C, ^{40}Ca, ^{56}Fe, ^{60}Ni, ^{66}Zn, ^{88}Sr, ^{92}Mo, ^{100}Mo and ^{138}Ba were reported in the 51–168 MeV energy range [18–21]. Finally, the elastic scattering of ^{16}C from ^{12}C at 260 MeV was acquired by Ogloblin *et al* [22].

Recently, Kaki [23] presented density distributions of the $^{10–14}$C and ^{16}C nuclei using the relativistic mean-field (RMF) results. He studied the reaction cross-sections of proton elastic scattering from carbon isotopes. However, a comprehensive and simultaneous microscopic analysis of the scattering cross-sections of the $^{10–14}$C and ^{16}C nuclei from different targets at various incident energies has not been done using the RMF density distribution.

In this study, we perform a detailed analysis of the elastic scattering angular distributions for the RMF density distributions of $^{10–14}$C and ^{16}C projectiles by 17 different targets from ^{12}C to ^{208}Pb in the energy region 29.1–650 MeV. The elastic scattering is known to be an efficient method in the investigation of density distributions. Then, we propose new and global potential sets

Published online: 08 August 2019

that show the relationship between the imaginary potential depths of all the nuclei and the theoretical results.

In §2, a brief summary of the theoretical analysis is provided. Section 3 presents the results and discussion. Section 4 gives a summary and conclusions.

2. Theoretical procedure

2.1 *Optical model analysis*

The optical model consisting of two potentials, the real and imaginary potentials, is one of the most efficient nuclear models used in obtaining elastic scattering cross-sections. The optical model analysis of the elastic scattering cross-sections for all the systems investigated in this work is carried out using two different model potentials: (i) the double-folding (DF) potential for the real part and the Woods–Saxon (WS) potential for the imaginary part and (ii) the DF potential for both real and imaginary parts. These model potentials are explained in the following subsections. The code FRESCO [24] is used to achieve the theoretical results.

2.1.1 *First approach* (*DF–WS*). One of the approaches used commonly to determine the real potential is the DF model [25–27]. The DF model calculates the real potential with the help of both projectile and target densities and nucleon–nucleon interaction. In this sense, the DF potential is written as

$$V_{\mathrm{DF}}^{\mathrm{M3Y}}(\mathbf{r}) = \int \mathrm{d}\mathbf{r}_1 \int \mathrm{d}\mathbf{r}_2 \rho_{\mathrm{P}}(\mathbf{r}_1)\rho_{\mathrm{T}}(\mathbf{r}_2)\nu_{\mathrm{NN}}(\mathbf{r}_{12}), \quad (1)$$

where $\mathbf{r}_{12} = \mathbf{r} - \mathbf{r}_1 + \mathbf{r}_2$, $\nu_{\mathrm{NN}}(\mathbf{r}_{12})$ is the effective NN interaction, $\rho_{\mathrm{P}}(\mathbf{r}_1)$ and $\rho_{\mathrm{T}}(\mathbf{r}_2)$ are the densities of the projectile and the target nuclei, respectively. The density distributions of the examined nuclei in our study are described in the next subsection. The M3Y nucleon–nucleon (Michigan 3 Yukawa) realistic interaction accepted for ν_{NN} [28] is presented as

$$\nu_{\mathrm{NN}}^{\mathrm{M3Y}}(r) = 7999\,\frac{\exp(-4r)}{4r} - 2134\,\frac{\exp(-2.5r)}{2.5r} - 276\,(1 - 0.005\epsilon_{\mathrm{Lab}})\delta(r), \quad (2)$$

where $\epsilon_{\mathrm{Lab}} = E/A$ is the incident energy per nucleon. The DF potential is determined using the code DFPOT [29].

The imaginary potential, which is the other part of the optical model, is considered as the WS potential with three free parameters in the following form:

$$W(r) = W_0 f(r), \quad f(r) = \frac{1}{1 + \exp(x_i)}, \quad (3)$$

$$x_i = \frac{r - R_w}{a_w}, \quad R_w = r_w(A_{\mathrm{P}}^{1/3} + A_{\mathrm{T}}^{1/3}), \quad (4)$$

where W_0, r_w and a_w for the imaginary potential are depth, radius and diffuseness parameters, respectively. By determining the real and imaginary potentials, the optical potential that is labelled as DF(R) in our study is obtained.

2.1.2 *Second approach* (*DF–DF*). For a comparative study, we use a second approach except for the above-mentioned procedure. In this approach, the real potential is thought as the DF potential. In addition to this, the imaginary potential is assumed as the DF potential multiplied by a renormalisation factor N_{I}. In this way, both real and imaginary potentials have the same shape but different strengths that is evaluated in the following form:

$$U(\mathrm{R}) = (N_{\mathrm{R}} + \mathrm{i}N_{\mathrm{I}})V_{\mathrm{DF}}(\mathrm{R}), \quad (5)$$

where N_{R} and N_{I} are the renormalisation factors for the real and imaginary potentials, respectively. The renormalisation factor (N_{R} or N_{I}) is a parameter evaluated to increase the agreement between the experimental data and the theoretical results for the DF model. However, V_{DF} is the DF potential that is calculated with M3Y nucleon–nucleon realistic interaction together with effective NN interaction [30]. In this case, the number of free parameters of the imaginary potential will be minimised. At the same time, the difficulty in selecting potential parameters will be eliminated while performing the theoretical analysis. This potential is exhibited as DF(R + I) in our work.

2.2 *Density distributions*

Density distribution is one of the most important parameters in the DF model calculations. The density distributions of $^{10-14}$C and ^{16}C projectiles are assumed to be RMF density distributions reported by Kaki [23]. Figure 1 shows a comparative representation of these density distributions and the density distribution is maximum at the centre then decreases towards the surface.

In the present analysis, 17 different nuclei from ^{12}C to ^{208}Pb as target nuclei are evaluated. In this context, two-parameter Fermi (2pF) density distribution is used to obtain densities of ^{27}Al, ^{28}Si, ^{40}Ca, ^{56}Fe, ^{58}Ni, ^{60}Ni, ^{66}Zn, ^{88}Sr, ^{90}Zr, ^{92}Mo, ^{100}Mo, ^{138}Ba and ^{208}Pb target nuclei:

$$\rho(r) = \frac{\rho_0}{1 + \exp((r - c)/z)}, \quad (6)$$

where values of ρ_0, c and z are displayed in table 1. The density distributions of ^{12}C and ^{16}O from other target

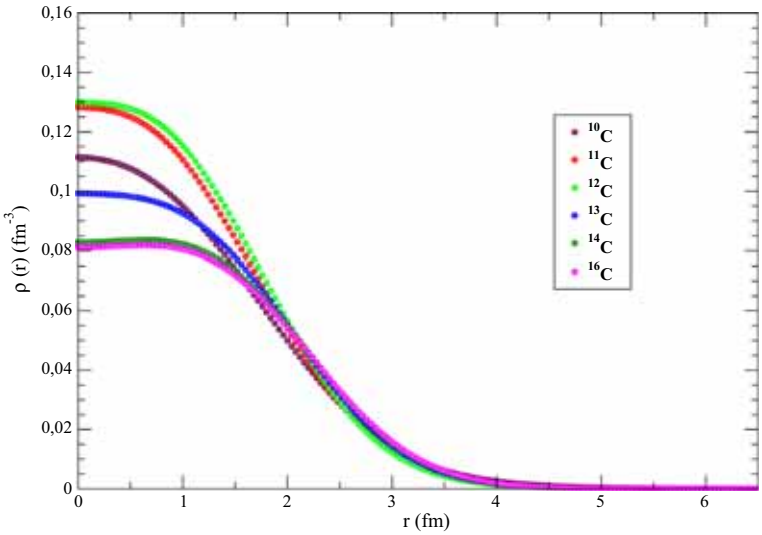

Figure 1. The RMF density distributions of $^{10–14}$C and ^{16}C projectiles.

Table 1. The parameters of two-parameter Fermi (2pF) density for the ^{27}Al, ^{28}Si, ^{40}Ca, ^{56}Fe, ^{58}Ni, ^{60}Ni, ^{66}Zn, ^{88}Sr, ^{90}Zr, ^{92}Mo, ^{100}Mo, ^{138}Ba, ^{208}Pb nuclei and the parameters of Gaussian density for the ^{12}C and ^{16}O nuclei.

2pF					Gaussian				
Nucleus	c	z	ρ_0	Ref.	Nucleus	ς	ϱ	β	Ref.
^{27}Al	2.84	0.569	0.2015	[31]	^{12}C	0.1644	0.082003	0.3741	[32]
^{28}Si	3.15	0.475	0.175	[32]	^{16}O	0.13173	0.085058	0.3228	[35–37]
^{40}Ca	3.60	0.523	0.169	[32]					
^{56}Fe	3.99561	0.5935	0.17209927	[33]					
^{58}Ni	4.094	0.54	0.172	[32]					
^{60}Ni	4.20	0.475	0.1716	[31]					
^{66}Zn	4.291	0.638	0.163819	[33]					
^{88}Sr	4.83	0.496	0.168971	[33]					
^{90}Zr	4.90	0.515	0.165	[32]					
^{92}Mo	4.83	0.540	0.173622	[34]					
^{100}Mo	4.98	0.540	0.173303	[34]					
^{138}Ba	5.60	0.540	0.171930	[34]					
^{208}Pb	6.62	0.551	0.1600	[31]					

nuclei are taken as Gaussian shape in the following form:

$$\rho(r) = (\varsigma + \varrho r^2)\exp(-\beta r^2), \tag{7}$$

where ς, ϱ and β are listed in table 1. The density of ^{14}N target nucleus is written as [38]

$$\rho_i(r) = \frac{\rho_{0i}}{1+\exp((r-R_{0i})/a_i)}, \tag{8}$$

where ρ_{0i} (the central density), R_{0i} (half-density radii) and a_i (the surface thickness parameter) are parameterised by

$$\rho_{0i} = \frac{3A_i}{4\pi R_{0i}^3}\left[1+\frac{\pi^2 a_i^2}{R_{0i}^2}\right]^{-1}, \tag{9}$$

$$R_{0i} = 0.90106 + 0.10957A_i - 0.0013A_i^2 + 7.71458\times10^{-6}A_i^3 - 1.62164\times10^{-8}A_i^4, \tag{10}$$

$$a_i = 0.34175 + 0.01234A_i - 2.1864\times10^{-4}A_i^2 + 1.46388\times10^{-6}A_i^3 - 3.24263\times10^{-9}A_i^4. \tag{11}$$

The density distribution of ^{13}C target nucleus is taken as the modified harmonic oscillator (MHO) density [39]

$$\rho(r) = \rho_0\left(1+\alpha\frac{r^2}{a^2}\right)\exp\left(-\frac{r^2}{a^2}\right), \quad \rho_0 = \frac{1+1.5\alpha}{(\sqrt{\pi}\alpha)^3}, \tag{12}$$

where $\alpha = 1.403$ and $a = 1.635$ [11].

3. Results and discussion

The suitability of the RMF densities in describing the elastic scattering cross-sections of six different carbon isotopes is studied. With this goal, the elastic scattering angular distributions of the $^{10-14}$C and ^{16}C nuclei consisting of 46 reactions including both DF(R) and DF(R + I) approaches at different incident energies are calculated. The results are shown in figures 2–11. Moreover, the imaginary potential equations for each carbon projectile are obtained by means of the RMF densities.

The depth (W_0), radius (r_w) and diffusion (a_w) of the WS potential of the imaginary part of the optical potential are sought to obtain a good harmony with the experimental data. The geometrical parameters (r_w and a_w) of each reaction that is searched in steps of 0.1 and 0.01 fm are given in tables 2–7. Then, W_0 values for

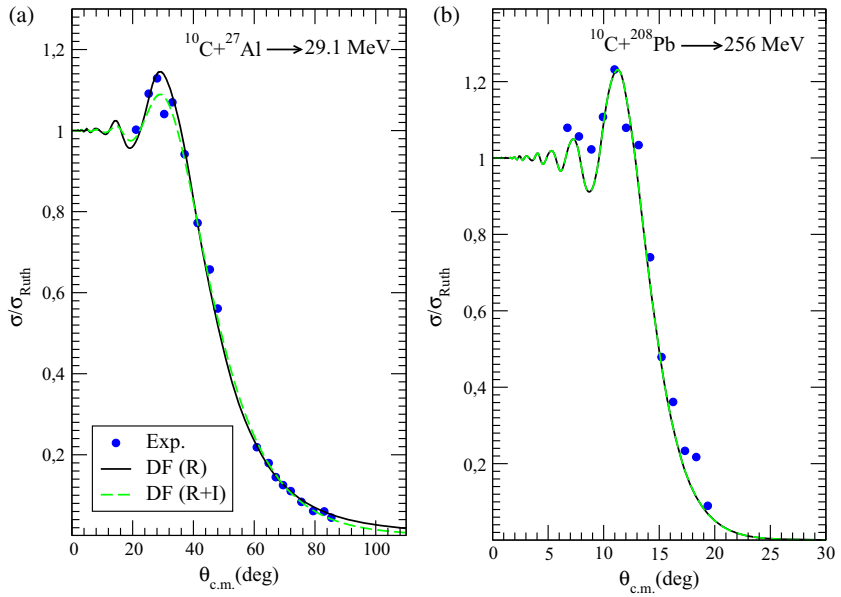

Figure 2. The elastic scattering angular distributions calculated using the RMF density of ^{10}C projectile for (**a**) ^{10}C + ^{27}Al at 29.1 MeV and (**b**) ^{10}C + ^{208}Pb at 256 MeV. The experimental data are taken from refs [8,9].

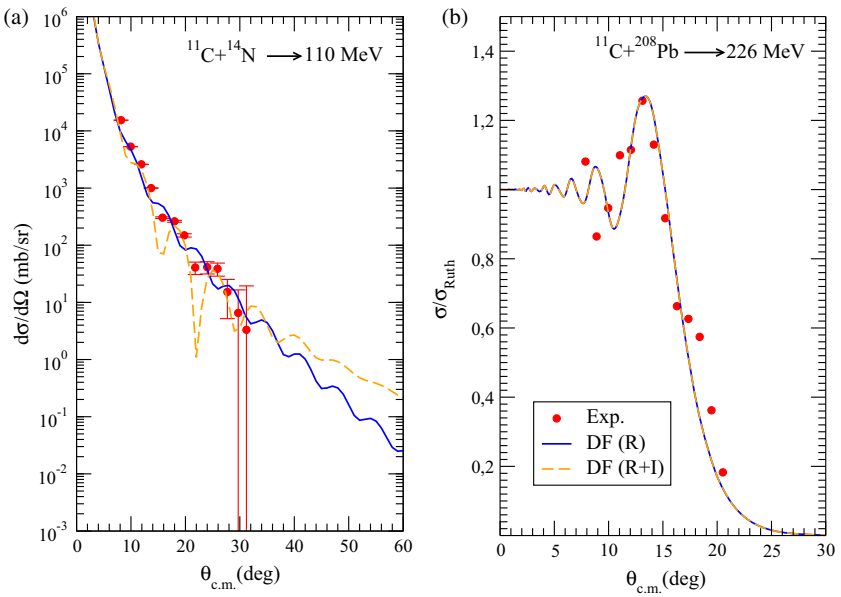

Figure 3. The elastic scattering angular distributions calculated using the RMF density of ^{11}C projectile for (**a**) ^{11}C + ^{14}N at 110 MeV and (**b**) ^{11}C + ^{208}Pb at 226 MeV. The experimental data are taken from refs [9,10].

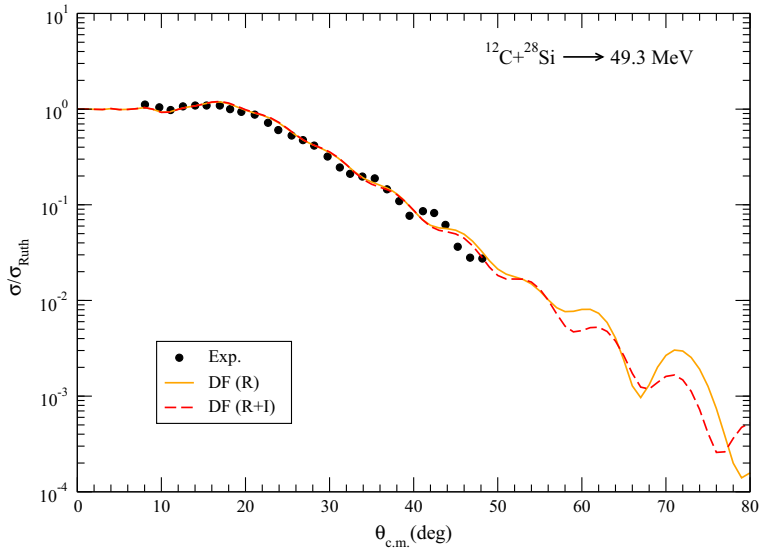

Figure 4. The elastic scattering angular distributions calculated using the RMF density of ^{12}C projectile for ^{12}C + ^{28}Si at 49.3 MeV. The experimental data are taken from ref. [11].

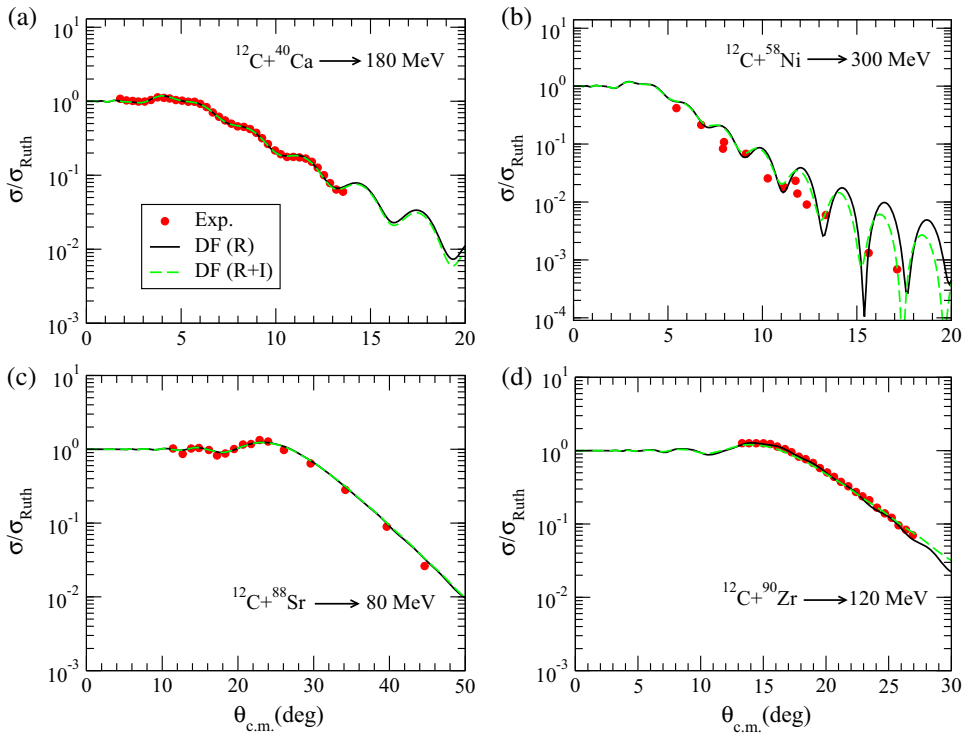

Figure 5. Same as figure 4, but for (**a**) ^{12}C + ^{40}Ca at 180 MeV, (**b**) ^{12}C + ^{58}Ni at 300 MeV, (**c**) ^{12}C + ^{88}Sr at 80 MeV and (**d**) ^{12}C + ^{90}Zr at 120 MeV. The experimental data are taken from refs [12–14].

constant values of r_w and a_w are examined and all the values are listed in tables 2–7. Finally, the other parameters calculated for all the investigated reactions in this work are the real (J_R) and imaginary (J_I) volume integrals in MeV fm^3. The values of J_R and J_I for each reaction are shown in tables 2–7.

3.1 *Analysis with ^{10}C projectile*

The elastic scattering cross-sections of ^{10}C + ^{27}Al (at 29.1 MeV) and ^{10}C + ^{208}Pb (at 256 MeV) reactions have been calculated using two different approaches of the optical model. The theoretical results, together with

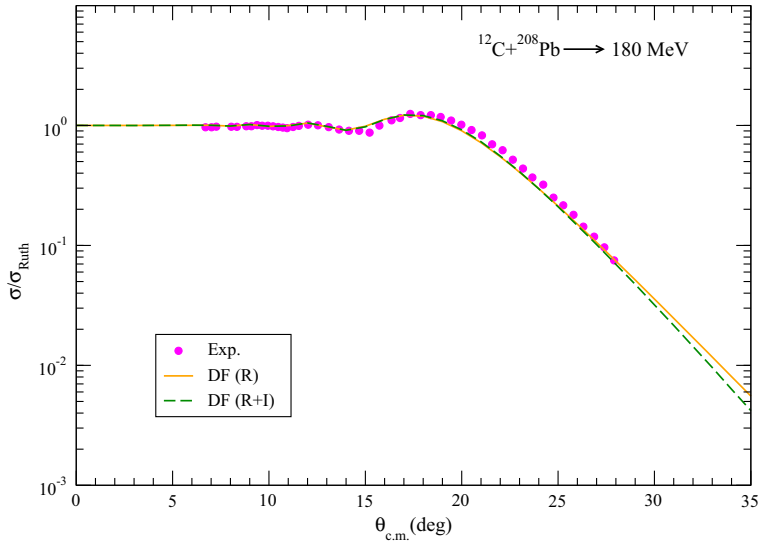

Figure 6. Same as figure 4, but for ^{12}C +^{208}Pb at 180 MeV. The experimental data are taken from ref. [12].

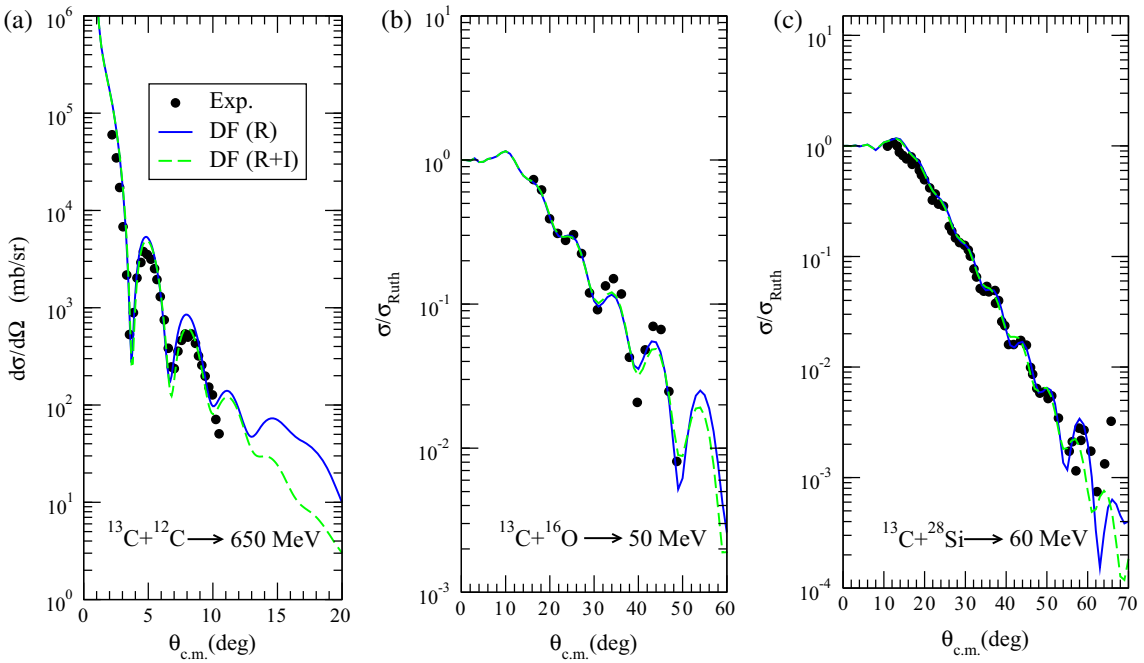

Figure 7. The elastic scattering angular distributions calculated using the RMF density of ^{13}C projectile for (**a**) ^{13}C + ^{12}C at 650 MeV, (**b**) ^{13}C + ^{16}O at 50 MeV and (**c**) ^{13}C + ^{28}Sr at 60 MeV. The experimental data are taken from refs [15–17].

the experimental data, are presented in figure 2. Also, the optical potential parameters of the analysed systems are given in table 2. It is observed that the harmony between the theoretical results and the experimental data is very good. Additionally, it is seen that the DF(R) result of ^{10}C + ^{27}Al reaction is slightly better than the DF(R+I) result. The renormalisation factor (N_R) shows the deviation from unity while the theoretical results with both DF(R) and DF(R+I) models are achieved. Also, the total reaction cross-sections (σ) of DF(R) and DF(R+I) models are provided in table 2. It is observed that the results of both models are very close to each other. The σ value of ^{10}C + ^{208}Pb reaction at 256 MeV is reported to be 3269 mb for the São Paulo potential (SPP) calculation in [9]. It can be said that our σ value is very close to the value in [9].

3.2 *Analysis with ^{11}C projectile*

For the analysis with ^{11}C projectile, we have investigated the elastic scattering angular distributions with the ^{14}N target nucleus at 110 MeV and the ^{208}Pb target

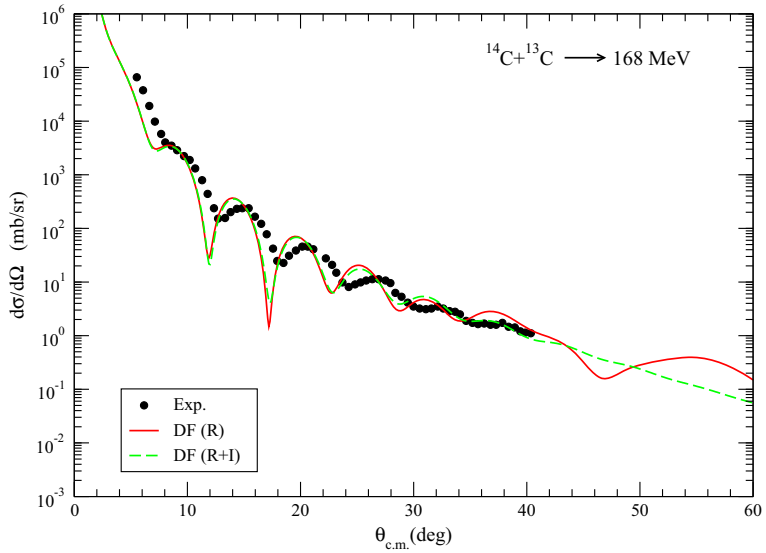

Figure 8. The elastic scattering angular distributions calculated using the RMF density of ^{14}C projectile for ^{14}C + ^{13}C at 168 MeV. The experimental data are taken from ref. [18].

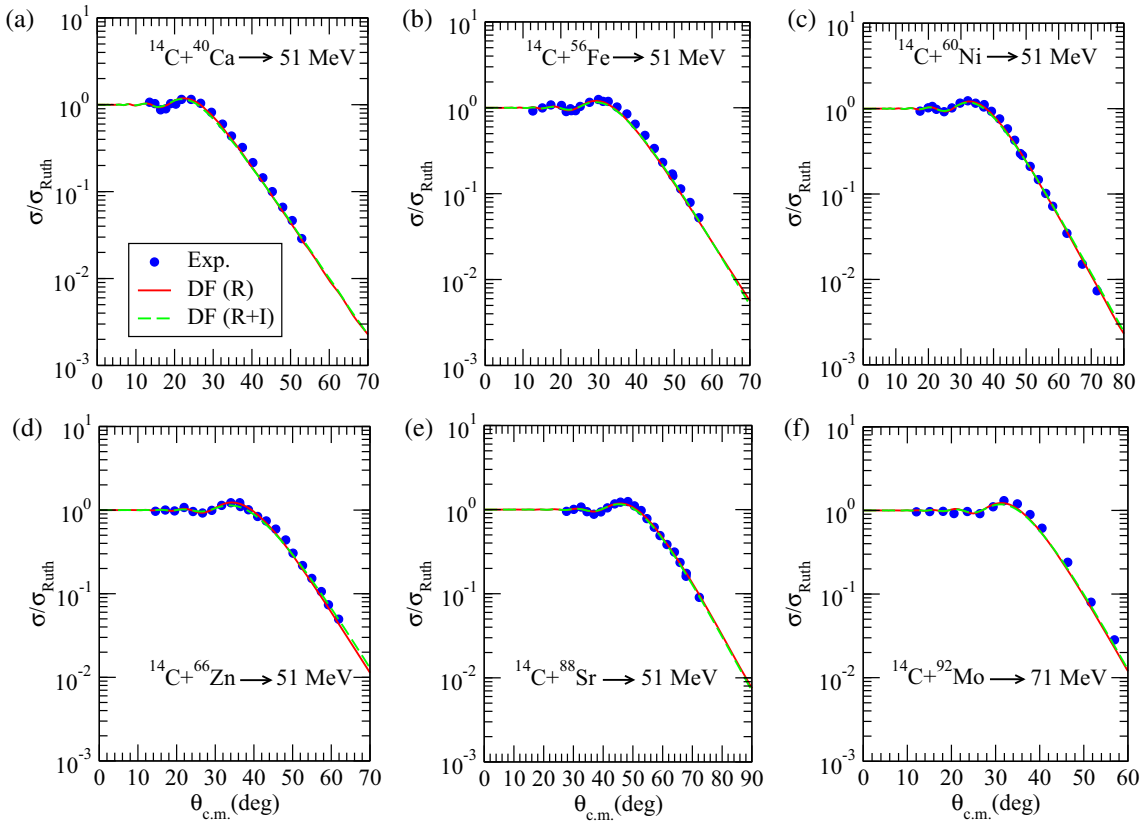

Figure 9. Same as figure 8, but for (**a**) ^{14}C + ^{40}Ca at 51 MeV, (**b**) ^{14}C + ^{56}Fe at 51 MeV, (**c**) ^{14}C + ^{60}Ni at 51 MeV, (**d**) ^{14}C + ^{66}Zn at 51 MeV, (**e**) ^{14}C + ^{88}Sr at 51 MeV and (**f**) ^{14}C + ^{92}Mo at 71 MeV. The experimental data are taken from refs [19,20].

nucleus at 226 MeV. We have compared our results with the experimental data in figure 3. We have observed that our results are in good agreement with experimental data. However, we have noticed that DF(R) and DF(R+I) results are slightly different for ^{11}C + ^{14}N reaction while they are the same for ^{11}C + ^{208}Pb reaction. We have listed the optical potential parameters in table 3. We have realised that the N_R values of

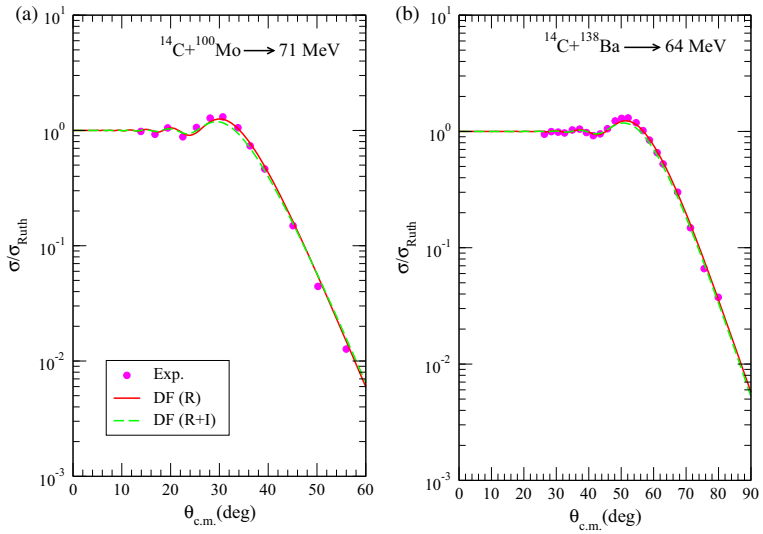

Figure 10. Same as figure 8, but for (**a**) $^{14}C + ^{100}Mo$ at 71 MeV and (**b**) $^{14}C + ^{138}Ba$ at 64 MeV. The experimental data are taken from refs [20,21].

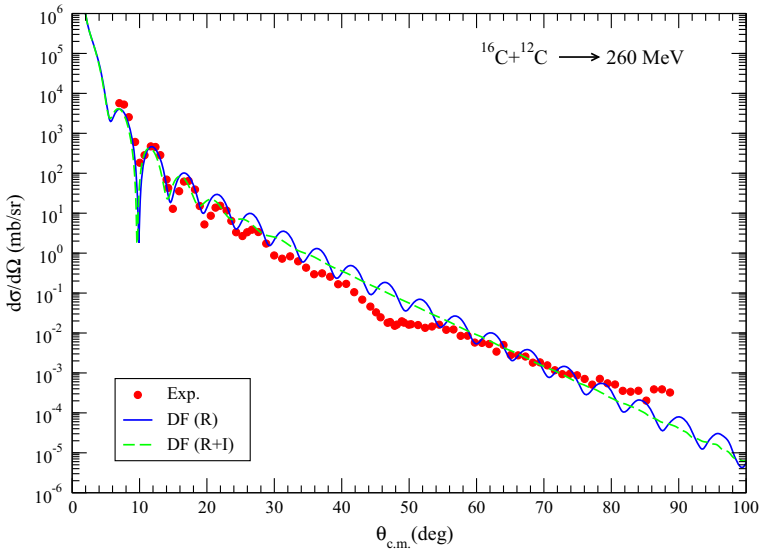

Figure 11. The elastic scattering angular distributions calculated using the RMF density of ^{16}C projectile for $^{16}C + ^{12}C$ at 260 MeV. The experimental data are taken from ref. [22].

DF(R) and DF(R+I) are ≈ 1 for $^{11}C + ^{14}N$ reaction while the N_R values deviate from unity for $^{11}C + ^{208}Pb$ reaction. For comparison with the literature, we have found the σ value of $^{11}C + ^{208}Pb$ as 3266 mb for the SPP calculation [9]. As a result, we can deduce that our result is in agreement with literature [9].

3.3 *Analysis with ^{12}C projectile*

The elastic scattering cross-sections of the ^{12}C nucleus by the ^{28}Si, ^{40}Ca, ^{58}Ni, ^{88}Sr, ^{90}Zr and ^{208}Pb target nuclei have been evaluated in three processes consisting of light target ($^{12}C + ^{28}Si$ at 49.3 MeV), medium-heavy target ($^{12}C + ^{40}Ca$ at 180 MeV, $^{12}C + ^{58}Ni$ at 300 MeV, $^{12}C + ^{88}Sr$ at 80 MeV and $^{12}C + ^{90}Zr$ at 120 MeV) and heavy target ($^{12}C + ^{208}Pb$ at 180 MeV) reactions. The theoretical results are exhibited in figure 4 for light target nucleus reaction, in figure 5 for medium-heavy target nucleus reactions and in figure 6 for heavy target nucleus reaction. In addition, the optical potential parameters are given in table 4. The theoretical results of light, medium and heavy target nucleus reactions are in very good agreement with each other and with experimental data. The N_R values of DF(R) and DF(R+I) models are unity. Also, the cross-sections of both models are listed in table 4. It is seen that the cross-sections are very close to each other. In [12], the σ values of $^{12}C + ^{40}Ca$, $^{12}C + ^{90}Zr$ and $^{12}C + ^{208}Pb$

Table 2. The normalisation factors (N_R and N_I), the depth (W_0) in MeV, real (J_R) and imaginary (J_I) volume integrals in MeV fm^3 and the cross-sections (σ) in mb obtained from analysis with DF(R) and DF(R + I) potentials of elastic scattering of ^{10}C from ^{27}Al (at 29.1 MeV) and ^{208}Pb (at 256 MeV). The geometrical parameters are fixed as follows: $r_w = 1.30$ fm, $a_w = 0.45$ fm and $r_c = 1.25$ fm.

System	$E_{\rm Lab}$	$N_{\rm R}^{\rm (R)}$	$W_0^{\rm (R)}$	$J_{\rm R}^{\rm (R)}$	$J_{\rm I}^{\rm (R)}$	$\sigma^{\rm (R)}$	$N_{\rm R}^{\rm (R+I)}$	$N_{\rm I}^{\rm (R+I)}$	$J_R^{\rm (R+I)}$	$J_{\rm I}^{\rm (R+I)}$	$\sigma^{\rm (R+I)}$
^{10}C+^{27}Al	29.1	0.72	19.5	298.7	95.0	879.9	0.42	0.55	174.2	228.1	968.6
^{10}C+^{208}Pb	256	0.87	20.0	334.3	47.5	3156.7	0.70	0.70	268.9	268.9	3287.4

Table 3. Same as table 2, but for ^{11}C elastic scattering by ^{14}N (at 110 MeV) and ^{208}Pb (at 226 MeV). The geometrical parameters are fixed as follows: $r_w = 1.30$ fm, $a_w = 0.58$ fm and $r_c = 1.25$ fm.

System	$E_{\rm Lab}$	$N_{\rm R}^{\rm (R)}$	$W_0^{(R)}$	$J_{\rm R}^{\rm (R)}$	$J_I^{\rm (R)}$	$\sigma^{\rm (R)}$	$N_{\rm R}^{\rm (R+I)}$	$N_{\rm I}^{\rm (R+I)}$	$J_{\rm R}^{\rm (R+I)}$	$J_{\rm I}^{\rm (R+I)}$	$\sigma^{\rm (R+I)}$
^{11}C+^{14}N	110	1.0	47.5	405.0	308.3	1820.9	1.0	0.47	405.0	190.3	1329.9
^{11}C+^{208}Pb	226	0.74	11.5	289.4	25.4	3120.3	0.8	0.60	312.8	234.6	3082.0

Table 4. Same as table 2, but for ^{12}C elastic scattering by ^{28}Si (at 49.3 MeV), ^{40}Ca (at 180 MeV), ^{58}Ni (at 300 MeV), ^{88}Sr (at 80 MeV), ^{90}Zr (at 120 MeV) and ^{208}Pb (at 180 MeV). The geometrical parameters are fixed as follows: $r_w = 1.24$ fm, $a_w = 0.60$ fm and $r_c = 1.25$ fm.

System	$E_{\rm Lab}$	$N_{\rm R}^{\rm (R)}$	$W_0^{\rm (R)}$	$J_{\rm R}^{\rm (R)}$	$J_{\rm I}^{\rm (R)}$	$\sigma^{\rm (R)}$	$N_{\rm R}^{\rm (R+I)}$	$N_{\rm I}^{\rm (R+I)}$	$J_{\rm R}^{\rm (R+I)}$	$J_{\rm I}^{\rm (R+I)}$	$\sigma^{\rm (R+I)}$
^{12}C+^{28}Si	49.3	1.0	11.5	414.0	44.6	1349.6	1.0	0.5	414.0	207.0	1334.6
^{12}C+^{40}Ca	180	1.0	25.3	397.6	83.8	2095.0	1.0	1.0	397.6	397.6	2092.9
^{12}C+^{58}Ni	300	1.0	18.5	384.4	52.6	2266.0	1.0	0.85	384.4	326.7	2327.5
^{12}C+^{88}Sr	80	1.0	13.5	410.5	32.8	1775.6	1.0	0.65	410.5	266.8	1794.7
^{12}C+^{90}Zr	120	1.0	13.5	406.5	32.5	2140.9	1.0	1.0	406.5	406.5	2321.5
^{12}C+^{208}Pb	180	1.0	32.0	398.8	58.6	3078.2	1.0	1.0	398.8	398.8	3058.3

Table 5. Same as table 2, but for ^{13}C elastic scattering by ^{12}C (at 650 MeV), ^{16}O (at 50 MeV) and ^{28}Si (at 60 MeV). The geometrical parameters are fixed as follows: $r_w = 1.28$ fm, $a_w = 0.60$ fm and $r_c = 1.25$ fm.

System	$E_{\rm Lab}$	$N_{\rm R}^{\rm (R)}$	$W_0^{\rm (R)}$	$J_{\rm R}^{\rm (R)}$	$J_{\rm I}^{\rm (R)}$	$\sigma^{\rm (R)}$	$N_{\rm R}^{\rm (R+I)}$	$N_{\rm I}^{\rm (R+I)}$	$J_{\rm R}^{\rm (R+I)}$	$J_{\rm I}^{\rm (R+I)}$	$\sigma^{\rm (R+I)}$
^{13}C+^{12}C	650	1.0	13.0	350.2	80.5	1334.9	1.0	0.75	350.2	262.6	1319.0
^{13}C+^{16}O	50	1.0	10.0	413.4	53.2	1419.3	1.0	0.60	413.4	248.0	1412.2
^{13}C+^{28}Si	60	1.0	12.0	413.4	48.6	1591.3	1.1	0.82	454.7	339.0	1664.4

Table 6. Same as table 2, but for ^{14}C elastic scattering by ^{13}C (at 168 MeV), ^{40}Ca (at 51 MeV), ^{56}Fe (at 51 MeV), ^{60}Ni (at 51 MeV), ^{66}Zn (at 51 MeV), ^{88}Sr (at 51 MeV), ^{92}Mo (at 71 MeV), ^{100}Mo (at 71 MeV) and ^{138}Ba (at 64 MeV). The geometrical parameters are fixed as follows: $r_w = 1.24$ fm, $a_w = 0.60$ fm and $r_c = 1.25$ fm.

System	$E_{\rm Lab}$	$N_{\rm R}^{\rm (R)}$	$W_0^{\rm (R)}$	$J_{\rm R}^{\rm (R)}$	$J_{\rm I}^{\rm (R)}$	$\sigma^{\rm (R)}$	$N_{\rm R}^{\rm (R+I)}$	$N_{\rm I}^{\rm (R+I)}$	$J_{\rm R}^{\rm (R+I)}$	$J_{\rm I}^{\rm (R+I)}$	$\sigma^{\rm (R+I)}$
^{14}C+^{13}C	168	1.0	14.1	402.5	73.6	1552.3	1.0	0.60	402.5	241.5	1518.3
^{14}C+^{40}Ca	51	1.0	25.3	413.2	76.3	1545.7	1.0	1.00	413.2	413.2	1643.2
^{14}C+^{56}Fe	51	0.71	22.0	294.1	57.5	1462.7	0.6	0.55	248.5	227.8	1524.2
^{14}C+^{60}Ni	51	1.0	16.5	414.1	42.0	1351.0	1.0	0.74	414.1	306.4	1406.2
^{14}C+^{66}Zn	51	0.63	19.5	261.2	47.7	1373.1	0.5	0.50	207.3	207.3	1508.8
^{14}C+^{88}Sr	51	1.0	19.5	414.7	42.7	1179.5	1.0	0.71	414.7	294.4	1232.4
^{14}C+^{92}Mo	71	0.9	21.5	371.5	46.3	1683.5	0.8	0.70	330.2	288.9	1746.0
^{14}C+^{100}Mo	71	1.0	20.0	412.8	41.8	1780.0	1.0	0.88	412.8	363.2	1932.2
^{14}C+^{138}Ba	64	1.0	15.5	413.7	29.0	1223.8	1.0	0.58	413.7	239.9	1308.0

Table 7. Same as table 2, but for ^{16}C elastic scattering by ^{12}C (at 260 MeV). The geometrical parameters are fixed as follows: $r_w = 1.12$ fm, $a_w = 0.425$ fm and $r_c = 1.25$ fm.

System	E_{Lab}	$N_{\mathrm{R}}^{(\mathrm{R})}$	$W_0^{(\mathrm{R})}$	$J_{\mathrm{R}}^{(\mathrm{R})}$	$J_{\mathrm{I}}^{(\mathrm{R})}$	$\sigma^{(\mathrm{R})}$	$N_{\mathrm{R}}^{(\mathrm{R+I})}$	$N_{\mathrm{I}}^{(\mathrm{R+I})}$	$J_{\mathrm{R}}^{(\mathrm{R+I})}$	$J_{\mathrm{I}}^{(\mathrm{R+I})}$	$\sigma^{(\mathrm{R+I})}$
^{16}C+^{12}C	260	1.03	95.5	408.5	345.6	1502.5	1.00	0.62	396.6	245.8	1730.0

reactions are reported as 2165, 2219 and 2873 mb, respectively. It can be predicted that these values are very close to our results. Consequently, it can be said that the theoretical results obtained for the RMF density distribution of ^{12}C projectile using the DF(R) and DF(R+I) models describe the experimental data very well.

3.4 *Analysis with ^{13}C projectile*

The elastic scattering angular distributions of $^{13}\mathrm{C}+^{12}\mathrm{C}$ (at 650 MeV), $^{13}\mathrm{C}+^{16}\mathrm{O}$ (at 50 MeV) and $^{13}\mathrm{C}+^{28}\mathrm{Si}$ (at 60 MeV) reactions have been calculated using the DF(R) and DF(R+I) models. The theoretical results have been compared with the experimental data in figure 7. It has been observed that the theoretical results of $^{13}\mathrm{C}+^{12}\mathrm{C}$, $^{13}\mathrm{C}+^{16}\mathrm{O}$ and $^{13}\mathrm{C}+^{28}\mathrm{Si}$ reactions are in good agreement with the experimental data. They provide correct descriptions of the minima and maxima. The N_{R} values of DF(R) and DF(R + I) models are ≈ 1. Additionally, the σ values of DF(R) and DF(R + I) models are given in table 5. It is seen that the σ values are in harmony with each other.

3.5 *Analysis with ^{14}C projectile*

The elastic scattering cross-sections of the ^{14}C nucleus on the ^{13}C, ^{40}Ca, ^{56}Fe, ^{60}Ni, ^{66}Zn, ^{88}Sr, ^{92}Mo, ^{100}Mo and ^{138}Ba target nuclei have been calculated in three processes consisting of light target ($^{14}\mathrm{C}+^{13}\mathrm{C}$ at 168 MeV), medium-heavy target ($^{14}\mathrm{C}+^{40}\mathrm{Ca}$ at 51 MeV, $^{14}\mathrm{C}+^{56}\mathrm{Fe}$ at 51 MeV, $^{14}\mathrm{C}+^{60}\mathrm{Ni}$ at 51 MeV, $^{14}\mathrm{C}+^{66}\mathrm{Zn}$ at 51 MeV, $^{14}\mathrm{C}+^{88}\mathrm{Sr}$ at 51 MeV and $^{14}\mathrm{C}+^{92}\mathrm{Mo}$ at 71 MeV) and heavy target ($^{14}\mathrm{C}+^{100}\mathrm{Mo}$ at 71 MeV and $^{14}\mathrm{C}+^{138}\mathrm{Ba}$ at 64 MeV) reactions. The theoretical results are shown in figure 8 for light target nucleus reaction, in figure 9 for medium-heavy target nucleus reactions and in figure 10 for heavy target nucleus reactions. The optical potential parameters for all the reactions are listed in table 6. The compatibility of the theoretical results of light, medium and heavy target nucleus reactions with the experimental data is very good. The N_{R} values of DF(R) and DF(R + I) models are around unity in general sense. Additionally, the σ values of DF(R) and DF(R + I) models are shown in table 6. It is observed that the two models also give similar descriptions of the scattering observables when the σ values of DF(R) and DF(R + I) models are compared. Consequently, it can be said that the RMF density of the ^{14}C nucleus is very successful in describing the elastic scattering cross-sections of light, medium and heavy target nucleus reactions from ^{13}C to ^{138}Ba.

3.6 *Analysis with ^{16}C projectile*

In our study, the last examined reaction is $^{16}\mathrm{C}+^{12}\mathrm{C}$ at 260 MeV. The elastic scattering cross-sections calculated using DF(R) and DF(R + I) approaches are presented and compared with the experimental data in figure 11. Also, the optical potential parameters are displayed in table 7. It is observed that the theoretical results of DF(R) and DF(R + I) models are in agreement with the data in the general sense although they miss some experimental data. The σ value of $^{16}\mathrm{C}+^{12}\mathrm{C}$ at 260 MeV is given as 1471 mb in [22]. This value is especially very consistent with the σ value of DF(R) approach.

3.7 *Derivation of new global potential sets*

One of the principal aims in nuclear reaction studies is considered to be the search for global potential sets. If this is achieved, a faster process can be performed when different systems are running. But it is not so simple. For this purpose, a large number of calculations are performed and the global potential sets are sought from the parameters obtained.

In the present study, we obtain new global potential sets for the analysed carbon isotopes. For this, we use the parameters that are obtained from the optical model calculations performed in this work. Thus, new global potential expressions for each carbon isotopes are found to be

for ^{10}C nucleus:

$$W_0^{(\mathrm{R})} = 18.292 - 0.01131861E + \frac{0.367326Z_{\mathrm{T}}}{A_{\mathrm{T}}^{1/3}}, \tag{13}$$

for ^{11}C nucleus:

$$W_0^{(\mathrm{R})} = 55.4055 + 0.0209124E - \frac{3.51393Z_{\mathrm{T}}}{A_{\mathrm{T}}^{1/3}}, \tag{14}$$

for ^{12}C nucleus:

$$W_0^{(\mathrm{R})} = 2.52069 + 0.0358592E + \frac{1.35853Z_{\mathrm{T}}}{A_{\mathrm{T}}^{1/3}}, \tag{15}$$

for ^{13}C nucleus:

$$W_0^{(\mathrm{R})} = 5.40296 + 0.00624627E + \frac{1.3496Z_\mathrm{T}}{A_\mathrm{T}^{1/3}}, \quad (16)$$

for ^{14}C nucleus:

$$W_0^{(\mathrm{R})} = 29.7451 - 0.0793482E - \frac{0.650275Z_\mathrm{T}}{A_\mathrm{T}^{1/3}}, \quad (17)$$

for ^{16}C nucleus:

$$W_0^{(\mathrm{R})} = 31.8333 + 0.122436E + \frac{12.1467Z_\mathrm{T}}{A_\mathrm{T}^{1/3}}, \quad (18)$$

where E is the incident energy of the $^{10-14}$C and ^{16}C nuclei, and Z_T and A_T are atomic and mass numbers of target nucleus, respectively. These global potential expressions can be evaluated to describe the scattering observables, because global potential parameters for the carbon isotopes are scarce. Thus, they will give an idea in those situations when there is a difficulty in examining the experimental data in a theoretical manner. Moreover, these expressions will accelerate the theoretical analysis.

4. Summary and conclusions

In this paper, we have studied the elastic scattering cross-sections of carbon isotopes $^{10-14}$C and ^{16}C from light to heavy targets at various incident energies. The theoretical results have been acquired using the DF model within the optical model. RMF density distributions have been used for $^{10-14}$C and ^{16}C projectiles. The results have provided a very good description of the experimental data.

We have also studied new global sets of the imaginary potentials of the analysed carbon isotopes which are necessary to practically get scattering observables. To achieve this, we have evaluated the potential parameters obtained from the calculations. We have given new potential sets for carbon isotopes. These potentials will play a key role for describing both nucleon–nucleus and nucleus–nucleus reactions like elastic and inelastic scatterings, nucleon transfer reactions, etc.

Acknowledgement

The author thanks the referee for valuable discussion and comments.

References

[1] M Aygun, *Eur. Phys. J. A* **48**, 145 (2012)
[2] M Aygun, I Boztosun and Y Sahin, *Phys. At. Nucl.* **75**, 963 (2012)
[3] M Aygun, *Ann. Nucl. Energy* **51**, 1 (2013)
[4] M Aygun, *Commun. Theor. Phys.* **60**, 69 (2013)
[5] M Aygun and I Boztosun, *Few-Body Syst.* **55**, 203 (2014)
[6] M Aygun, *Pramana – J. Phys.* **88**: 53 (2017)
[7] A N Abdullah, *Pramana – J. Phys.* **89**: 43 (2017)
[8] E F Aguilera *et al*, *IOP Conf. Ser. J. Phys. Conf. Ser.* **876**, 012001 (2017)
[9] Y Y Yang *et al*, *Phys. Rev. C* **90**, 014606 (2014)
[10] X Tang *et al*, *Phys. Rev. C* **67**, 015804 (2003)
[11] R M De Vries, D A Goldberg, J W Watson, M S Zisman and J G Cramer, *Phys. Rev. Lett.* **39**, 450 (1977)
[12] C C Sahm *et al*, *Phys. Rev. C* **34**, 2165 (1986)
[13] H G Bohlen, H Ossenbrink, H Lettau and W von Oertzen, *Z. Phys. A – Atoms Nucl.* **320**, 237 (1985)
[14] G Ingold, H G Bohlen, M Clover, H Lettau, H Ossenbrink and W von Oertzen, *Z. Phys. A – Atoms Nucl.* **305**, 135 (1982)
[15] N Ikeda *et al*, *Eur. Phys. J. A* **7**, 491 (2000)
[16] T Yamaya *et al*, *Phys. Rev. C* **37**, 2585 (1988)
[17] C Berat *et al*, *Nucl. Phys. A* **555**, 455 (1993)
[18] M McCleskey *et al*, *AIP Conf. Proc.* **1213**, 225 (2010)
[19] O Hansen, F Videbæk, E R Flynn, J C Peng and J A Cizewski, *Nucl. Phys. A* **364**, 145 (1981)
[20] W Mayer *et al*, *Phys. Rev. C* **26**, 500 (1982)
[21] F Videbæk, O Hansen, B S Nilsson, E R Flynn and J C Peng, *Nucl. Phys. A* **433**, 457 (1985)
[22] A A Ogloblin *et al*, *Phys. Rev. C* **62**, 044601 (2000)
[23] K Kaki, *Prog. Theor. Exp. Phys.* **96**, 093D01 (2017)
[24] I J Thompson, *Comput. Phys. Rep.* **7**, 167 (1988)
[25] F Pakdel, A A Rajabi and L Nickhah, *Pramana – J. Phys.* **87**: 90 (2016)
[26] M Aygun, *Chin. J. Phys.* **53**, 080301 (2015)
[27] M Aygun, Y Kucuk, I Boztosun and A A Ibraheem, *Nucl. Phys. A* **848**, 245 (2010)
[28] G R Satchler and W G Love, *Phys. Rep.* **55**, 183 (1979)
[29] J Cook, *Comput. Phys. Commun.* **25**, 125 (1982)
[30] M Y M Hassan, M Y H Farag, E H Esmael and H M Maridi, *Phys. Rev. C* **79**, 064608 (2009)
[31] S Hossain, M N A Abdullah, Md Zulfiker Rahman, A K Basak and F B Malik, *Phys. Scr.* **87**, 015201 (2013)
[32] M El-Azab Farid and M A Hassanain, *Nucl. Phys. A* **678**, 39 (2000)
[33] C W De Jager, H De Vries and C De Vries, *At. Data Nucl. Data Tables* **14**, 479 (1974)
[34] W Zou, Y Tian and Z Yu Ma, *Phys. Rev. C* **78**, 064613 (2008)
[35] G Kocak, M Karakoc, I Boztosun and A B Balantekin, *Phys. Rev. C* **81**, 024615 (2010)
[36] S Qing-Biao, F Da-Chun and Z Yi-Zhong, *Phys. Rev. C* **43**, 2773 (1991)
[37] H F Ehrenberg *et al*, *Phys. Rev.* **113** 666 (1959)
[38] R K Gupta, D Singh and W Greiner, *Phys. Rev. C* **75**, 024603 (2007)
[39] A Mehndiratta and P Shukla, *Nucl. Phys. A* **961**, 22 (2017)